



Proceeding Paper

Energy Harvesting for a Microscale Biosensing Device via Piezoelectric Micromachined Ultrasonic Transducers [†]

Alexandru Paolo Mardare *, Mamoun Morh and Aldo Ghisi 🗅

Department of Civil and Environmental Engineering, Politecnico di Milano, Piazza Leonardo da Vinci 32, 20133 Milano, Italy; mamoun.morh@mail.polimi.it (M.M.); aldo.ghisi@polimi.it (A.G.)

- * Correspondence: alexandrupaolo.mardare@polimi.it
- † Presented at the 12th International Electronic Conference on Sensors and Applications (ECSA-12), 12–14 November 2025; Available online: https://sciforum.net/event/ECSA-12.

Abstract

Microdevices with dimensions comparable to a blood cell, i.e., tens of micrometers, show great potential for use in the human body. They can be adopted to identify the source of diseases, track their evolution and enhance the effectiveness of therapies, significantly improving patients' quality of life. A key challenge is how to power the devices, which should ideally be obtained wireless from a remote source. Piezoelectric micromachined ultrasonic transducers (pMUTs) offer a solution thanks to their ability to generate and collect energy via acoustic waves. In this work, numerical simulations of transmitter pMUT arrays are performed with the aim of generating an acoustic wave synchronized with a single pMUT or pMUT array receiver. The latter is intended for insertion in the human body. The characteristics required to switch on and power nano-electronics, in terms of generated voltage and electrical power at the receiver, are studied in ballistic gel, a material that mimics human organs. Focus is on a bio-compatible material for the piezoelectric layer, aluminum nitride enriched with scandium. Coupled electromechanical and acoustic simulations show that, of the considered pMUT devices, an 8 × 8 transmitter array combined with a single-device receiver (with a 50 μ m pitch) or a 2 \times 2 receiver array provide alternative options, with each offering advantages in terms of voltage amplitude or power at steady state. The overall dimension of the receiver, at maximum only $100 \times 100 \,\mu\text{m}^2$, is compatible with a future proof-of-concept biosensing platform test chip.

Keywords: pMUT; wireless energy transfer; biosensors; numerical simulation



Academic Editor: Firstname Lastname

Published:

Citation: Mardare, A.P.; Morh, M.; Ghisi, A. Energy Harvesting for a Microscale Biosensing Device via Piezoelectric Micromachined Ultrasonic Transducers. *Eng. Proc.* 2025, 1, 0. https://doi.org/

Copyright: © 2025 by the authors. Licensee MDPI, Basel, Switzerland. This article is an open access article distributed under the terms and conditions of the Creative Commons Attribution (CC BY) license (https://creativecommons.org/licenses/by/4.0/).

1. Introduction

Microscale biosensing devices have rapidly emerged as a fundamental medical tool for health monitoring, dramatically enhancing the effectiveness of therapies [1]. Recent advances in biomedicine and microelectronics, that brought the development of medical implants with dimensions in the tens-of-micrometers scale, require the identification of efficient, wireless, and miniaturized energy sources that can substitute conventional batteries, which are bulky and have limited lifespan.

These miniaturized devices have ground-breaking applications in dry eye disease treatment [3], cancer tracking, diagnosis [4,5] and cure of brain disorders [6], non-invasive, real-time monitoring [7,8] of metabolites, biomarkers, drugs and pathogens, aimed to identify the source and to track the evolution of diseases [9]. First, ultrasound waves are a more safe and efficient transmission medium, compared to electromagnetic waves,

Eng. Proc. 2025, 1, 0 https://doi.org/10.3390/0

Eng. Proc. 2025, 1, 0 2 of 13

having higher safe exposure limits and shorter wavelengths, that enable deeper penetration in the human body and, consequently, higher derivable power to the biosensing device. In addition to that, thin-film piezoelectric layers are able to efficiently convert acoustic energy into electrical energy despite their miniaturized size. This characteristic allows to design microscale devices that work at frequencies in the megahertz range, providing high operational speed and optimal coupling with high impedance fluids. Lastly, the choice of scandium aluminum nitride (ScAlN) as piezoelectric material, over the commonly used lead zirconate titanate (PZT), makes the device bio- and CMOS-compatible, ideal for the design of microscale biosensors. Piezoelectric Micromachined Ultrasonic Transducers (pMUTs) [10,11] represent a promising solution for energy harvesting of biomedical devices for multiple reasons [12,13].

In this paper, numerical simulations of one of the $Sc_{0.15}Al_{0.85}N$ pMUTs reported in [14] are carried out, to evaluate the operating frequency, the derivable power and the voltage of the selected devices, and to understand the energy harvesting capabilities of receivers with very small area, in the order of $100 \times 100 \ \mu m^2$. The analysis is conducted coupling the pMUT with ballistic gel, reported in [17], that most closely mimics the acoustic properties of the relevant human tissue.

The remainder of the contribution is arranged as follows. Section 2 discusses the selected device, describing its geometrical parameters, piezoelectric properties and design frequency, together with details related to the numerical simulation. In Section 3, frequency domain analyses are presented to evaluate the performance of the transmitter (Tx) (8 \times 8 array) and of the receiver (Rx), along with studies on crosstalk effects and acoustic coupling. Section 4 presents a time domain analysis of the whole setup, where Tx and Rx are placed 5 mm distant from each other in ballistic gel, to compute the collected voltage and the derivable power. The Section also discusses some fundamental aspects related to human tissue, such as acoustic attenuation of the material and safe exposure limits. In Section 5, final conclusions are drawn along with further developments of the current work. Used abbreviations are collected at the end of the paper.

2. Description of the pMUT Devices and Numerical Setup

In [14], six different $Sc_{0.15}Al_{0.85}N$ pMUTs are presented: three devices are designed for air-coupled applications, while the other three are designed for water-coupled applications. Being the ballistic gel a high impedance acoustic medium, comparable to water, the last three pMUTs are ideal for the required application. Among these devices, the smallest one, called R19 (labeled by its cavity radius), has been chosen to comply with the Rx area constraints ($100 \times 100 \ \mu m^2$). The selected device features a square pitch with a side length of $L_{pitch} = 50 \ \mu m$, meaning that it is possible to employ a 2 \times 2 array as the Rx, enhancing the collected energy and power, reducing the overall impedance of the device and enabling larger transmit power in case the signal is sent back. The cross section of the R19 pMUT is depicted in Figure 1.

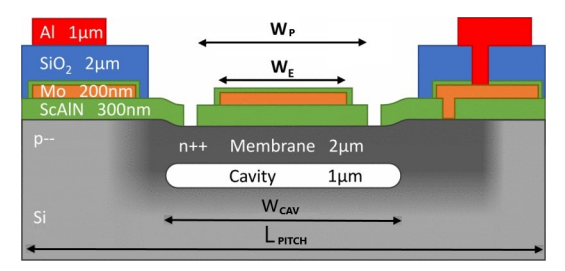


Figure 1. Cross section area of the device (adapted from [14]).

Eng. Proc. 2025, 1, 0 3 of 13

Its multi-layered structure is composed of a monocrystalline silicon (Si) substrate, etched to insert a cavity of 1 μ m and a Si membrane of 2 μ m. Selective areas of the Si layer are locally doped with phosphorous, setting the bottom surface of the piezoelectric layer to ground and avoiding the design of a metal bottom electrode. Then, a ScAlN layer of 300 nm and a molybdenum (Mo) layer, that acts as the top electrode, of 200 nm are deposited on the silicon membrane. To protect the Mo electrode from oxidation due to exposure to the external environment, an additional 50 nm coating layer of piezoelectric material is applied. Lastly, silicon dioxide (SiO₂) is deposited and etched to serve as insulation layer for aluminum (Al) tracks, which act as parallel interconnections for all pMUTs: SiO₂ and Al will not be considered for the numerical simulations, since they do not influence the pMUT dynamics.

With the exception of the Si pitch that has a square shape, the different layers are designed as sides of a square with rounded corners. The diameters of each layer are summarized in Table 1.

Table 1. Geometrical parameters of the R19 device. The Si membrane has the same width of the cavity, while W_P is computed as 70 % of W_{CAV} .

Device	W_{CAV} ($\mu \mathrm{m}$)	W_E (μ m)	$W_{\mathbf{P}}$ (μ m)
R19	38	26	26.6

The R19 pMUT has been modeled in COMSOL Multiphysics® to evaluate its design frequency and to check, through a transient analysis over time, the operating conditions from Tx to Rx in a ballistic gel medium. In the following subsections, the materials, the boundary conditions in all three physical domains (mechanical, electrical, acoustical), and the mesh requirements for the three-dimensional analysis are summarized.

Materials

In the mechanical domain, the R19 pMUT materials have been defined in the following way: Mo is isotropic elastic, Si and SCAIN are anisotropic elastic, ScAIN is also linearly piezoelectric. For the first two materials, the elastic constants (Si) and the Young's modulus (Mo) are extracted according to [15].

The $Sc_{0.15}Al_{0.85}N$ parameters, i.e., the elastic constants and the piezoelectric coupling coefficients, are instead computed following the methodology reported in [16], with the values summarized in Table 2.

Table 2. Material properties of $Sc_{0.15}Al_{0.85}N$, with $C_{66} = \frac{1}{2}(C_{11} - C_{12})$.

Property	Value	Unit
Dielectric constant ε_{33}	13.79	_
Mass density ρ	3.23	g/cm ³
Piezoelectric coefficient e_{31}	-0.63	C/m^2
Piezoelectric coefficient e_{33}	1.77	C/m^2
Piezoelectric coefficient e_{15}	-0.29	C/m^2
Elastic compliance C_{11}	348.97	GPa
Elastic compliance C_{12}	144.97	GPa
Elastic compliance C_{13}	119.68	GPa
Elastic compliance C_{33}	305.95	GPa
Elastic compliance C_{44}	104.82	GPa
Elastic compliance C_{66}	102.00	GPa

Eng. Proc. 2025, 1, 0 4 of 13

Boundary Conditions

Two types of analysis have been performed in the ballistic gel medium: frequency analysis and transient analysis.

In the first case, the acoustic domain has been approximated by a quarter sphere (see Figure 2(left)), with the device located at the center of the sphere, receiving or emitting an acoustic wave. If the device is the Tx, a time-varying voltage is applied and the pressure spectrum generated at a certain distance in the fluid is recorded. If the device is the Rx, a time-varying sinusoidal pressure is applied to the top of the sphere and the effect on the device, i.e., voltage and energy per pressure unit, generated across the piezoelectric layer, is recorded.

In the transient analysis case, the acoustic domain is instead approximated by a quarter cylinder (see Figure 2(right)).

In both cases, it is important to apply a spherical wave radiation condition on the outer (curved) surfaces to avoid spurious reflections of the acoustic wave. Moreover: symmetry is also exploited wherever possible in the mechanical and electrical domains (see Figure 2(center)); the device base under the cavity is held fixed; the displacement components in directions perpendicular to the lateral surfaces that are not on the symmetry planes are set to zero; the bottom and top surfaces of the piezoelectric layer are kept at zero voltage or at varying sinusoidal voltage, respectively.

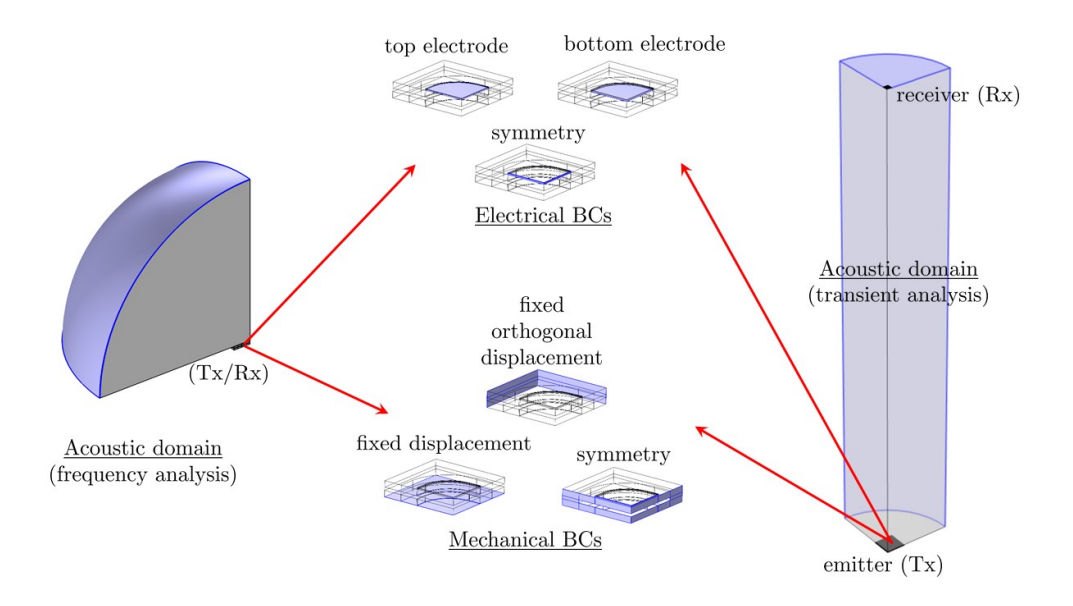


Figure 2. Acoustic domain for (**left**) frequency domain analysis and (**right**) transient analysis; (**center**) electrical and mechanical boundary conditions for a single pMUT. The analyses exploit symmetry wherever possible.

Meshing

To reduce the computational burden, in the mechanical domain only the piezoelectric layer has been discretized using three-dimensional, quadratic prismatic Lagrangian solid elements, while the other thin layers have been modeled using cubic (third-order) Lagrangian shell elements, according to the hybrid solid shell technique [18,19].

In the acoustic domain, tetrahedral quadratic Lagrangian elements are employed, with a maximum lateral size set to one-fifth of the acoustic wavelength. This meshing strategy ensures a spatial resolution of approximately 10 nodes per wavelength, which is sufficient for accurate wave propagation modeling. It is in fact very important to carefully design the mesh within the available memory and CPU power limits, since the fluid domain discretization can easily consume all computing resources: in the frequency

Eng. Proc. 2025, 1, 0 5 of 13

domain simulations 190,467 elements and 499,429 degrees of freedom (dofs) have been used, while in the transient analyses 410,104 elements and 756,605 dofs. The wall-clock time for the longest transient analyses has amounted to about 10 h with a workstation Intel® Xeon® W-2275 CPU @ 3.30GHz and 128 GB RAM.

3. Frequency Domain Analysis in Ballistic Gel

The eigen-frequency analysis considers all coupled domains. First, the focus is on the Tx, where a pMUT array is considered to achieve a relevant pressure wave amplitude at regime. Then, the analysis moves to the Rx, for which, in the case of the R19 device, the single configuration and the 2×2 array (giving a $100\times 100~\mu\text{m}^2$ footprint) are compared.

Transmit Sensitivity of the 8 \times 8 R19 Array

In this work, it is assumed conventionally that the frequency response function of an array is computed as the average center displacement of the individual membranes. This approach actually implies that all pMUT elements are actuated simultaneously and in phase and the excitation is spatially uniform across the array. The last hypothesis is actually challenged by the interaction between pMUTs, that cause nonlinear mechanical vibrations, and the acoustic cross-talk.

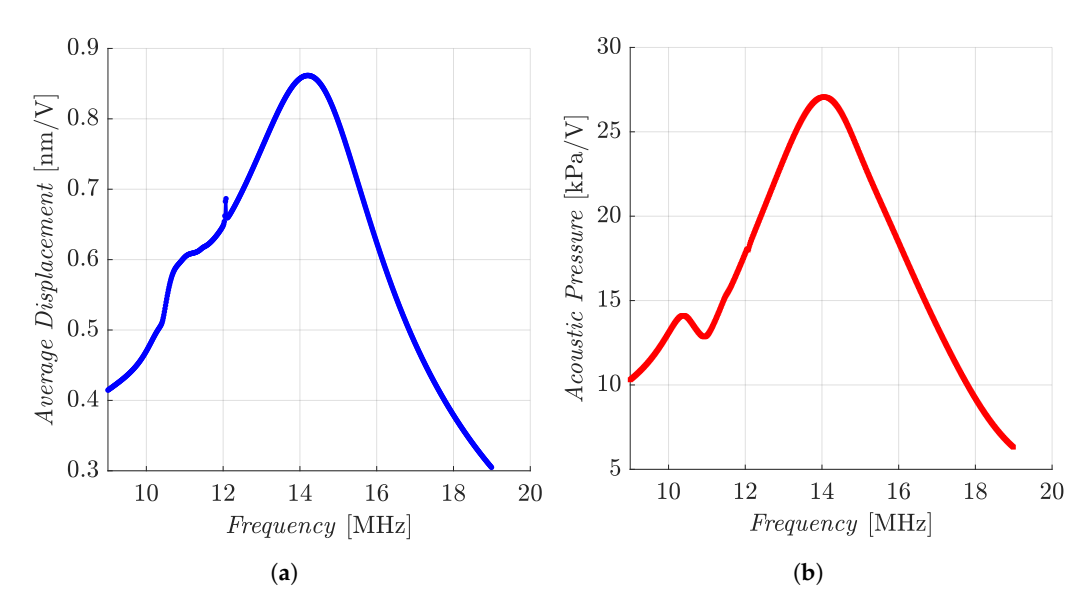


Figure 3. Tx (a) displacement and (b) acoustic pressure spectrum for the R19 8×8 array measured at a distance of 5 wavelengths in the gel medium.

The resonance peak shifts from 11.04 MHz for a single pMUT (not represented here) to 14.0 MHz for the 8 \times 8 array. This shift is primarily attributed to cross-talk phenomena, where mutual interactions between adjacent pMUT elements influence the overall dynamic behavior of the array (stiffening effect). The obtained fundamental frequency is comparable with the experimental results shown in [14] for a larger 50×55 R19 array. In the figure, in particular, the numerical resonance frequencies of the fundamental mode for a single R19 (in blue) and for a 2 \times 2 R19 array (in green) are indicated by dashed lines. The experimental measurements were carried out by using laser Doppler vibrometry (LDV, black line) and by a hydrophone (red line) which was placed at a distance of 20 mm in water. Although the dimensions of the measured array are much larger than those studied by numerical simulations, the results are encouraging when considering that the medium has a comparable velocity of propagation.

Eng. Proc. 2025, 1, 0 6 of 13

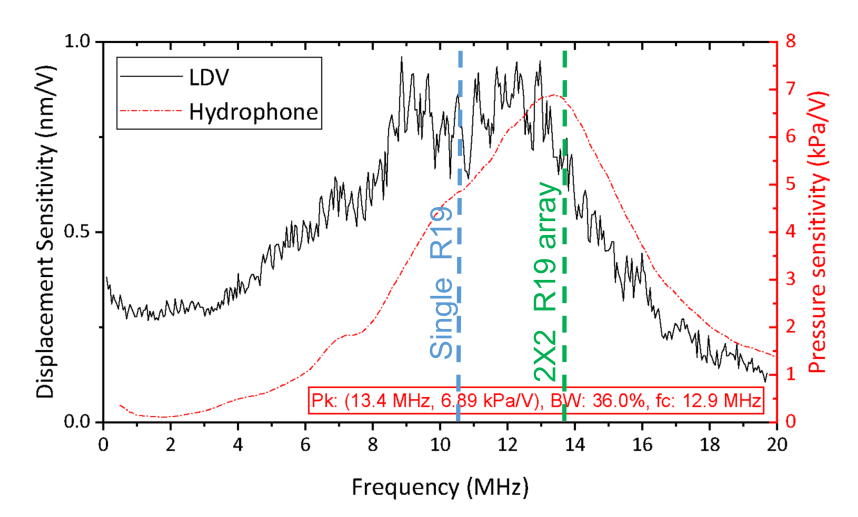


Figure 4. Experimental measurements of the response for a (large) R19 array, modified from [14].

Receiving Sensitivity of a Single R19 Device and of a 2×2 *R19 Array*

As depicted in Figure 5a, when the single R19 pMUT is deformed by an acoustic wave traveling in ballistic gel with an amplitude of 1 kPa at 10.5 MHz, due to the converse piezoelectric effect it generates an AC voltage amplitude of about 1.4 mV on the top electrode, and the piezoelectric layer produces an energy peak of 1.25×10^{-4} fJ.

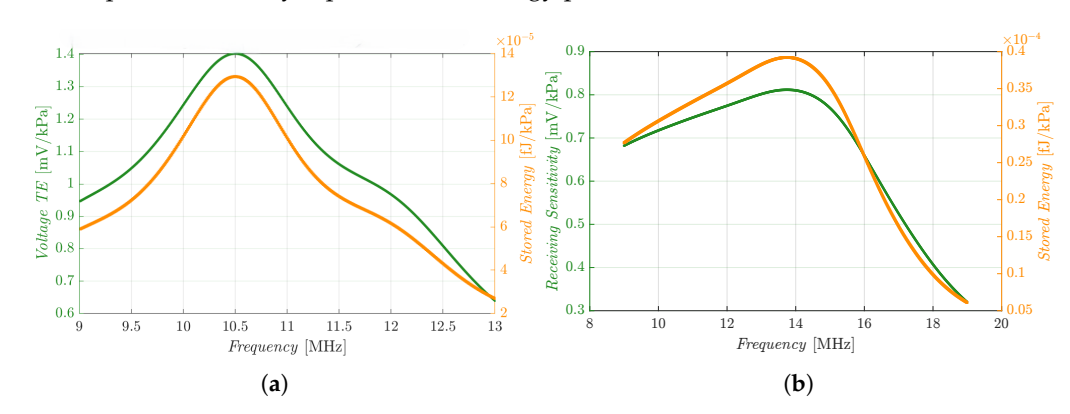


Figure 5. Rx sensitivity of (a) a single R19 device and (b) a 2×2 array of R19 devices in gel.

When the 2 \times 2 array, instead, is deformed by the same acoustic wave, each elements generates a 0.8 mV-amplitude voltage and stores energy with a 0.4 \times 10⁻⁴ fJ peak (1.6 \times 10⁻⁴ fJ if we consider the whole array). The cross-talk effect of the array can be observed, as the generated voltage is decreased with respect to the single device. On the other hand, by connecting the four pMUTs in parallel, it is possible to harvest more energy and power, and also to reduce the overall impedance.

Several aspects must be considered to define the optimal set-up for energy harvesting, specifically regarding the operational frequencies of the two device configurations:

- The 2×2 array allows for better resonance frequency matching with the Tx, as both are affected by stiffening effects that cause a frequency shift. Better matching provides lower losses in the transmit sensitivity (the operational frequency is always set to the resonance of the Rx);
- Higher operational frequency (2×2 array case) brings higher collected power, being this term dependent on the frequency, ideal for energy harvesting;
- However, the ballistic gel attenuation must be considered for our analysis. This term also depends on the operational frequency, meaning that, in the case of a single R19

Eng. Proc. 2025, 1, 0 7 of 13

as Rx, there will be less attenuation and consequently reduced losses in the acoustic pressure, see also the discussion in the next Section;

- Spatial peak temporal average intensity must be checked, in order to respect the safety limits on ultrasound waves imposed by the United States Food and Drug Administration (FDA). On this topic, a lower transmit power, given by a higher frequency shift between Tx and Rx (single pMUT case), may be ideal to not overcome the FDA safety limits;
- In case the electrical signal must be delivered back from the Rx to the Tx, the 2 × 2 array seems more ideal for this purpose, because it brings more transmit power and it is better matched with the Tx.

As some points mentioned above contradict each other, a time domain analysis, described in the following Section, is also carried out. It will provide a detailed insight into all these topics in order to find the optimal configuration for our purpose.

4. Time Domain Analysis

The time domain analysis has been carried out for the single R19 device and for the 2×2 array by placing the Tx and the Rx at a distance of 5 mm in the ballistic gel medium. A sinusoidal voltage, with 20 V amplitude and frequency equal to the Rx resonance, has been applied to the 8×8 array working as Tx, driving each element in phase. The analysis has been conducted for $5 \, \mu s$.

Figure 6 shows the results obtained in terms of voltage, energy, and power, when the 2×2 array is used as the Rx. Considering the ballistic gel speed of sound and the distance between the two devices, the acoustic wave is expected to reach the Rx after 3.16 μ s, consistent with what is depicted in the plots. The same analysis has been repeated for the single R19 used as Rx, with the results depicted in Figure 7. The peak values of the electrical parameters, at steady-state, are summarized in Table 3.

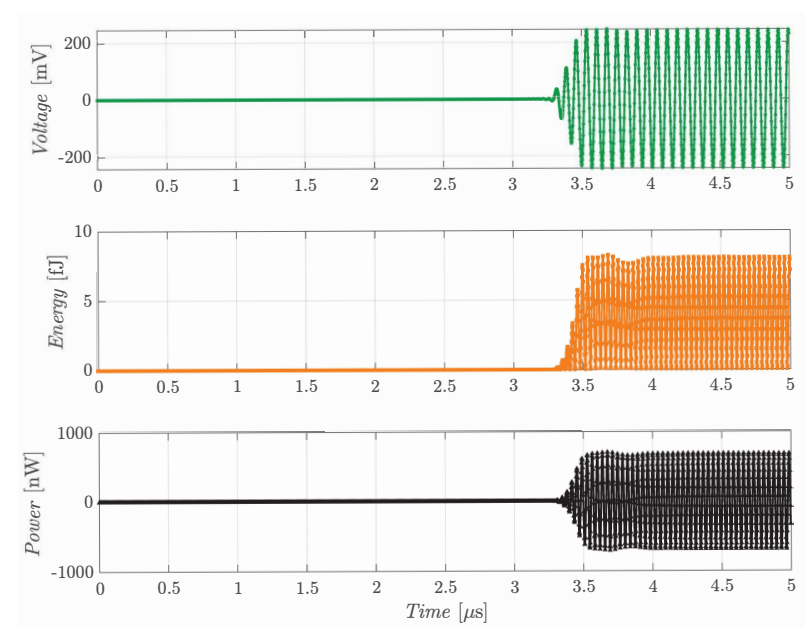


Figure 6. Voltage, energy and power measured over time by the piezoelectric layer at the R19 2 \times 2 array (Rx), as the R19 8 \times 8 array (Tx) emits waves at a distance of 5 mm.

Eng. Proc. 2025, 1, 0 8 of 13

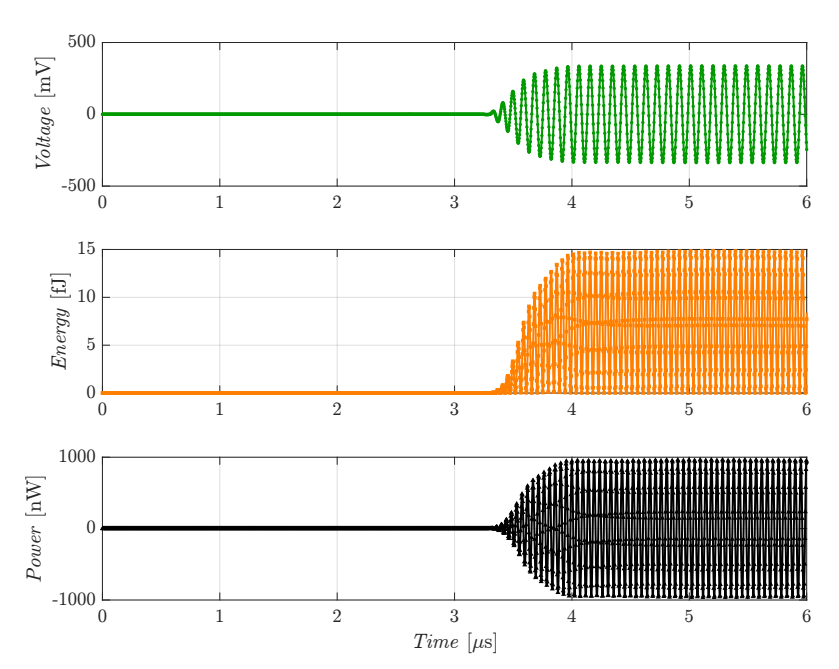


Figure 7. Voltage, energy and power measured over time by the piezoelectric layer at the single R19 (Rx), as the R19 8×8 array (Tx) emits waves at a distance of 5 mm.

Table 3. Extracted electrical performance from the transient simulation for the single R19 and the 2×2 array. In the latter case, a parallel connection between each element is considered.

Quantity	Symbol	Single R19	2 × 2 Array	Unit
Voltage	$V_{ m peak}$	337	213	mV
Energy	$E_{\rm peak}$	15	32.2	fJ
Power	$P_{ m peak}$	0.96	2.74	μW

Comparing the two voltage plots in Figures 6 and 7, it can be observed that the single R19 is able to collect a higher voltage, suggesting that the cross-talk effect of the 2×2 array brings a larger voltage drop compared to the frequency shift of the single device. The large bandwidth of the R19 in ballistic gel (\sim 4 MHz in the 8×8 array) facilitates operation at lower frequencies without considerable losses in the acoustic pressure. The two plots also evidence that the connection of four pMUTs in parallel enables a larger total stored energy. From these assumptions, it can be stated that the optimal configuration for the Rx initially depends on what is considered more fundamental for the target application, either voltage or electrical power. However, further aspects must be taken into account to find the ideal implementation, that will be analyzed in detail in the following subsection.

Output Power

The instantaneous output collected power is a crucial parameter for energy harvesting applications and can be computed as

$$P(t) = \frac{dE(t)}{dt},$$

indicating that it is directly dependent on the stored energy. More precisely, power can be approximated, starting from the energy formula $E(t) \approx \frac{1}{2} C_0 V(t)^2$, in the following way:

$$P(t) \propto C_0 V^2 \omega_0,\tag{1}$$

Eng. Proc. 2025, 1, 0 9 of 13

where C_0 is the capacitance of the piezoelectric layer at rest, V is the voltage amplitude detected and ω_0 is the angular resonance frequency. The above equation proves that both energy and power depend on C_0 (and therefore on the area and thickness of the piezoelectric layer) and V(t), while the latter term also depends on the fundamental frequency $f_0 = \frac{\omega_0}{2\pi}$. As a consequence, the 2 \times 2 array provides even more output power, having a higher working frequency, combined with the additional factor 4 given by the parallel connection. It must be specified that the formulae presented are an approximation of energy and power and are only used to demonstrate their dependence on voltage and frequency.

Time to Reach the Steady-State Condition

Another fundamental advantage of a higher resonance frequency lies in the settling time, which leads to increased operating speed. Indeed, by assuming the mechanical vibration of the membrane as that of a linear resonator, its time constant can be derived as

$$\tau = \frac{2Q}{\omega_0},$$

where Q is the quality factor. The time constant defines the steady-state condition ($\sim 5\tau$), meaning that the 2 \times 2 array will have a shorter settling time. Additionally, the array also presents a larger bandwidth compared to the single device, that leads to a lower quality factor, further reducing the settling time and, consequently, enabling faster operation for the 2 \times 2 array Rx.

Ballistic Gel Attenuation

Despite the advantages, higher working frequencies bring several drawbacks. A crucial one is the ballistic gel attenuation, that can be expressed as:

Attenuation (dB) =
$$\alpha \cdot f_0 \cdot d$$
, (2)

where α is the acoustic attenuation coefficient, set to $\alpha = 1.07$ dB/MHz · cm [17], and d is the distance, in centimeters, from the acoustic source. Since both Rxs operate at significantly high frequencies (>10 MHz), the pressure losses caused by the acoustic attenuation will be substantial, with a slightly larger dissipation in the 2 × 2 array.

As a first approximation, the pressure loss has been estimated analytically using Equation (2) and converting the attenuation from dB to linear, obtaining 47.6 % in the single R19 and 57 % in the 2×2 array case.

The peak values obtained by applying the respective reduction factors are reported in Table 4.

Table 4. Extracted electrical performance of the two Rxs when the ballistic gel acoustic attenuation is applied.

Quantity	Symbol	Single R19	2 × 2 Array	Unit
Voltage	$V_{ m peak}$	176.6	91.6	mV
Energy	$E_{ m peak}$	4.11	5.95	fJ
Power	$P_{ m peak}$	264	507	nW

Spatial Peak Temporal Average Intensity

As described in the previous section, the FDA has established an exposure limit to ultrasound waves in the medical field, specifically 7.2 mW/mm² [20]; to check whether an

experimental setup respects the defined safety limits, the Spatial Peak Temporal Average Intensity I_{SPTA} is computed at the point of maximum intensity [12]:

$$I_{\text{SPTA}} = \frac{p_{peak}^2}{2\rho c} \cdot C,\tag{3}$$

where p_{peak} is the measured peak acoustic pressure, C is the duty cycle and c, ρ are the ballistic gel speed of sound and density, respectively. The I_{SPTA} is practically defined as the ratio between the acoustic power $\frac{p_{peak}^2}{2}$ and the acoustic impedance $Z_a = \rho c$, multiplied by the signal duty cycle. The point of maximum intensity has been selected based on the Rayleigh distance, that establishes when the acoustic signal enters the far-field region and becomes stable. The Rayleigh distance Z is computed as follows [13]:

$$Z = \frac{a^2}{\lambda},\tag{4}$$

where a is the Tx radius and λ is the acoustic signal wavelength. Considering the 8×8 array Tx, where the radius a is evaluated as $a=\frac{7L_{pitch}}{2}=175~\mu\text{m}$, the Rayleigh distance turns out to be $Z=210~\mu\text{m}$ and $Z=273~\mu\text{m}$ for the single device case and for 2×2 array, respectively.

Based on the computed values, the maximum intensity point has been chosen at a distance of 500 μ m from the Tx, ensuring that the acoustic signal is completely stable. To evaluate the maximum I_{SPTA} , the acoustic pressure at the selected point has been measured in both cases during the transient analysis, obtaining the time-dependent plots depicted in Figure 8.

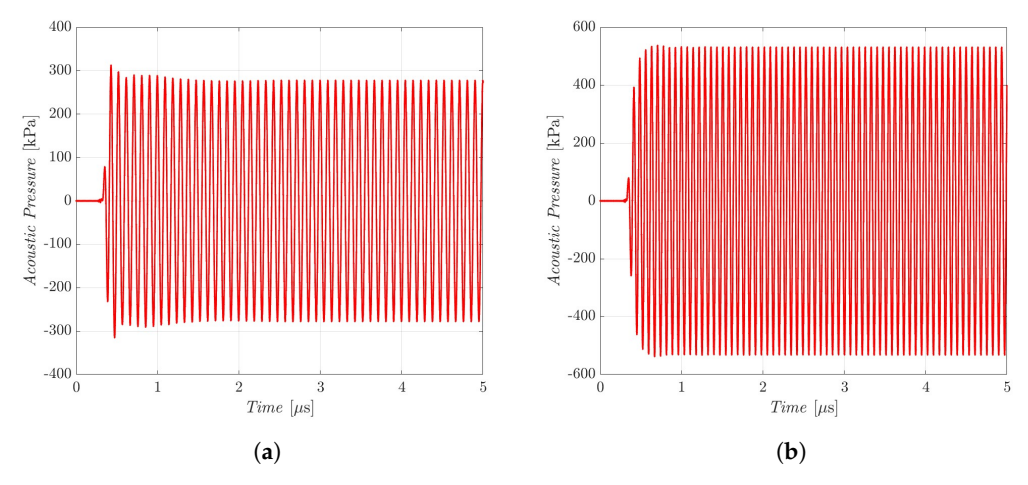


Figure 8. Acoustic pressure measured at 0.5 mm distance from the TX for (a) a single R19 device and (b) a 2×2 array.

Since the two Rxs work at different frequencies, the emitted pressure of the 8 \times 8 array will be different in the two case studies, with a higher acoustic pressure in the 2 \times 2 array case, as its resonance frequency is closer to the Tx one. As a result, it has been measured a peak pressure of 277 and 531 kPa, that corresponds to an I_{SPTA} of 23.5 and 86.5 mW/mm², respectively, above the FDA exposure limit. To solve this issue, a duty cycle C must be added to the driving input signal, namely 30% in the single R19 and 8% in the 2 \times 2 array case.

The main drawback given by the introduction of a duty cycle is the reduction of the average output collected energy, which decreases proportionally to *C*. The instantaneous power, instead, that has been measured during the transient analysis, is not affected by the duty cycle, resulting in an unchanged power peak. Considering the average energy and the voltage amplitude, the single R19 device appears to be more advantageous in this regard,

as it delivers a higher output compared to the 2×2 array. Conversely, looking at the instantaneous power, the 2×2 array performs better. More accurate numerical simulations, including the addition of a resistive load, will be conducted in the future to evaluate the average harvested power and quantify the reduction introduced by the duty cycle.

5. Conclusions

In this work, a pMUT device that exists in the literature has been studied as a harvester to provide wireless energy transmission to a biosensor through multi-physics three-dimensional simulations. Unlike previous studies, the present work has pursued the possibility of using high frequencies (>10 MHz) and a very small footprint ($100 \times 100 \, \mu m^2$). The analyses collected here propose a comparison between a single device and a 2×2 array for the receiver, both powered by an 8×8 array at a distance of 5 mm in a ballistic gel medium that mimics human internal organs.

By combining frequency response and transient analyses while accounting for acoustic dissipation phenomena, the study underscores the necessity for a trade-off between the single device and the array solution for the receiver: the former provides a higher voltage amplitude at steady-state, while the latter provides a higher instantaneous power. The single device performances, in particular, appear in line with digital nano-electronics requirements, also in case a duty cycle must be accounted for. The chosen material, ScAlN, replaces the more common PZT, which performs better under the same conditions; however, ScAlN guarantees better bio-compatibility and CMOS-integration. In addition, common PZT pMUT geometries [18] work at lower frequencies (1-5 MHz), where attenuation is significantly reduced. Ongoing work is exploring alternative but slightly larger geometries that could achieve a good performance balance, to have a precise comparison with PZT pMUTs in energy harvesting capabilities.

Author Contributions: Conceptualization and methodology, all; software and validation, A.P.M. and M.M.; writing—original draft preparation, A.P.M. and A.G.; writing—review and editing, all; visualization, A.P.M. and M.M.; supervision, A.G. All authors have read and agreed to the published version of the manuscript.

Funding: This study has been carried out within the MicroBioNIC project within the PRIN 2022 program (D.D. 104 - 02/02/2022 Ministero dell'Università e della Ricerca). This manuscript reflects only the authors' views and opinions and the Ministry cannot be considered responsible for them.

Institutional Review Board Statement: Not applicable.

Informed Consent Statement: Not applicable.

Data Availability Statement: Data can be obtained by kindly writing to the corresponding author.

Conflicts of Interest: The authors declare no conflicts of interest.

Abbreviations

The following abbreviations are used in this manuscript.

Al aluminum

CMOS complementary metal-oxide semiconductor

FDA Food and Drug Administration

Mo molybdenum

pMUT piezoelectric micromachined ultrasonic transducer

PZT lead zirconate titanate

Rx receiver

ScAlN scandium aluminium nitride

Si monocrystalline silicon

SiO₂ silicon dioxide Tx transmitter

References

1. Moisello, E.; Novaresi, L.; Sarkar, E.; Malcovati, P.; Costa, T.L.; Bonizzoni, E. PMUT and CMUT Devices for Biomedical Applications: A Review. *IEEE Access* **2024**, 12, 18640–18657. https://doi.org/10.1109/ACCESS.2024.3359906.

- 2. Zhang, L.; Du, W.; Kim, J.-H.; Yu, C.-C.; Dagdeviren, C. An Emerging Era: Conformable Ultrasound Electronics. *Adv. Mater.* **2024**, 36, 2307664. https://doi.org/10.1002/adma.202307664.
- 3. Wang, D.; Ji, Y.; Wang, S.; Lyu, H.; Zhang, S. Demonstration of MHz Piezoelectric Micromachined Ultrasonic Transducers (PMUTs) Array and the Potential Application in Biomedical Therapies. In Proceedings of the 2024 IEEE 37th International Conference on Micro Electro Mechanical Systems (MEMS), Austin, TX, USA, 21–25 January 2024; pp. 955–958. https://doi.org/10.1109/MEMS58180.2024.10439433.
- 4. Cai, J.; Gao, F.; Wang, Y.; Jiang, D.; Gu, Y.; Lou, L.; Wu, T. Photoacoustic Imaging Based on Broadened Bandwidth Aluminum Nitride Piezoelectric Micromachined Ultrasound Transducers. *IEEE Sens. Lett.* **2023**, 7, 2500604. https://doi.org/10.1109/LSENS. 2023.3254593.
- 5. Ledesma, E.; Uranga, A.; Torres, F.; Barniol, N. Fully Integrated Pitch-Matched AlScN PMUT-on-CMOS Array for High-Resolution Ultrasound Images. *IEEE Sens. J.* **2024**, 24, 15954–15966. https://doi.org/10.1109/JSEN.2024.3385911.
- Furukawa, R.; Yoshikawa, T.; Murakami, S.; Tateno, T. A Piezoelectric Micromachined Ultrasound Transducer Combined with Recording Electrodes for Acute Brain Preparations In Vitro. *J. Neurosci. Methods* 2024, 403, 110048. https://doi.org/10.1016/j.jneumeth.2023.110048.
- 7. Roy, K.; Kalyan, K.; Ashok, A.; Shastri, V.; Jeyaseelan, A.A.; Mandal, A.; Pratap, R. A PMUT Integrated Microfluidic System for Fluid Density Sensing. *J. Microelectromech. Syst.* **2021**, *30*, 642–649. https://doi.org/10.1109/JMEMS.2021.3091651.
- 8. Yang, L.; Zhang, J.; Zhang, L.; Zong, J.; Ren, H.; Lou, L. Novel Application of ScAlN PMUT for Intravenous Infusion Drip Monitoring. Sens. Actuators A Phys. 2025, 386, 116326. https://doi.org/10.1016/j.sna.2025.116326.
- 9. S, A.; Krishnan, K.; Arora, M. Review of pMUTs for medical imaging: Towards high frequency arrays. *Biomed. Phys. Eng. Express* **2023**, *9*, 022001. https://doi.org/10.1088/2057-1976/acaab2.
- 10. Qiu, Y.; Gigliotti, J.V.; Wallace, M.; Griggio, F.; Demore, C.E.M.; Cochran, S.; Trolier-McKinstry, S. Piezoelectric Micromachined Ultrasound Transducer (PMUT) Arrays for Integrated Sensing, Actuation and Imaging. *Sensors* **2015**, *15*, 8020–8041. https://doi.org/10.3390/s150408020.
- 11. Roy, K.; Lee, J.E.-Y.; Lee, C. Thin-film PMUTs: A review of over 40 years of research. *Microsyst. Nanoeng.* **2023**, *9*, 95. https://doi.org/10.1038/s41378-023-00555-7.
- 12. Rong, Z.; Zhang, M.; Ning, Y.; Pang, W. An Ultrasound-Induced Wireless Power Supply Based on AlN Piezoelectric Micromachined Ultrasonic Transducers. *Sci. Rep.* **2022**, *12*, 16174. https://doi.org/10.1038/s41598-022-19693-5.
- 13. Li, J.; Gao, Y.; Zhou, Z.; Ping, Q.; Qiu, L.; Lou, L. Piezoelectric Micromechanical Ultrasonic Transducer-Based Power-Harvesting Device for Wireless Power Transmission. *Micromachines* **2024**, *15*, 624. https://doi.org/10.3390/mi15050624.
- 14. Choong, D.S.W.; Chen, D.S.-H.; Goh, D.J.; Liu, J.; Ghosh, S.; Koh, Y.; Sharma, J.; Merugu, S.; Quaglia, F.; Ferrera, M.; et al. Silicon-On-Nothing ScAlN pMUTs. In Proceedings of the 2021 IEEE International Ultrasonics Symposium (IUS), Xi'an, China, 11–16 September 2021; pp. 1–4. https://doi.org/10.1109/IUS52206.2021.9593461.
- 15. Ghosh, S.; Ramegowda, P.C.; Goh, D.J.; Sharma, J.; Koh, Y.; Lee, J.E.-Y. Extraction of Material Properties of A Thin Silicon Membrane Embedded in A Piezoelectric Stack. In Proceedings of the 2023 IEEE International Ultrasonics Symposium (IUS). 2023, pp. 1–4. https://doi.org.10.1109/IUS51837.2023.10306882...
- 16. Ambacher, O.; Christian, B.; Feil, N.; Urban, D.F.; Elsässer, C.; Prescher, M.; Kirste, L. Wurtzite ScAlN, InAlN, and GaAlN crystals, a comparison of structural, elastic, dielectric, and piezoelectric properties. *J. Appl. Phys.* **2021**, *130*, 045102. https://doi.org/10.1063/5.0048647.
- 17. Alves, N.; Kim, A.; Tan, J.; Hwang, G.; Javed, T.; Neagu, B.; Courtney, B.K. Cardiac Tissue-Mimicking Ballistic Gel Phantom for Ultrasound Imaging in Clinical and Research Applications. *Ultrasound Med. Biol.* **2020**, *46*, 2057–2069. https://doi.org/10.1016/j.ultrasmedbio.2020.03.011.
- 18. Abdalla, O.M.O.; Massimino, G.; Savoia, A.S.; Quaglia, F.; Corigliano, A. Efficient Modeling and Simulation of PMUT Arrays in Various Ambients. *Micromachines* **2022**, *13*, 962. https://doi.org/10.3390/mi13060962.

19. Abdalla, O.M.O.; Garroni, M.G.; Moretti, E.; Massimino, G.; Corigliano, A.; Frangi, A.; Parolini, N.; Mazzieri, I.; Antonietti, P.; Giusti, D.; et al. Efficient Modeling and Simulation of Large PMUT Arrays for Biomedical Applications. In Proceedings of the 26th International Conference on Thermal, Mechanical and Multi-Physics Simulation and Experiments in Microelectronics and Microsystems (EuroSimE), Utrecht, The Netherlands, 6–9 April 2025; pp. 1–5. https://doi.org/10.1109/EuroSimE65125.2025.11 006590.

 Ballo, A.; Grasso, A.D.; Privitera, M. A High Efficiency and High Power Density Active AC/DC Converter for Battery-Less US-Powered IMDs in a 28-nm CMOS Technology. IEEE Access. 2024, 12, 7063-7070. https://doi.org/10.1109/ACCESS.2024.3351934.

Disclaimer/Publisher's Note: The statements, opinions and data contained in all publications are solely those of the individual author(s) and contributor(s) and not of MDPI and/or the editor(s). MDPI and/or the editor(s) disclaim responsibility for any injury to people or property resulting from any ideas, methods, instructions or products referred to in the content.